5272 *Chem. Mater.* **2009,** *21,* 5272–5283
DOI:10.1021/cm902344b

CHEMISTRY OF MATERIALS
Article

# Mn-Rich $BaMn_{1-x}Fe_xO_{3-\delta}$ Perovskites Revisited: Structural, Magnetic, and Electrical Properties of Two New 6H′ Polytypes

Laura Miranda,[†,‡] Derek C Sinclair,[‡] María Hernando,[†] Aurea Varela,[†] Alain Wattiaux,[§] Khalid Boulahya,[†] Jose M. González-Calbet,[†] and Marina Parras*[,†]

[†]*Departamento de Química Inorgánica, Facultad de Químicas, Universidad Complutense de Madrid, E-28040-Madrid, Spain.,* [‡]*Department of Engineering Materials, University of Sheffield, Mappin Street, Sheffield, S1 3JD, U.K., and* [§]*Institut de Chimie de la Matière Condensée de Bordeaux, ICMCB/UPR9048/CNRS, 87 avenue du Docteur A. Schweitzer 33608 Pessac*

*Received July 30, 2009. Revised Manuscript Received September 17, 2009*

The crystal and magnetic structures and electrical properties of two new Mn-rich 6H′-type hexagonal perovskites in the $BaMn_{1-x}Fe_xO_{3-\delta}$ system have been investigated. Structural characterization performed by X-ray, electron, and neutron diffraction and high resolution electron microscopy indicates that both $BaMn_{0.85}Fe_{0.15}O_{2.87}$ and $BaMn_{0.6}Fe_{0.4}O_{2.72}$ crystallize in the 6H′ hexagonal polytype ($P\bar{6}m2$ space group). The structure is formed by tetramers and dimers of face-sharing octahedra that are linked by corners. The anion deficiency is located at random through the hexagonal layers and increases with the Fe-content. In both phases, the central position of the tetramers is fully occupied by Mn, the remaining Mn and Fe cations being randomly distributed over different polyhedra. The Mössbauer spectroscopy data show Fe to be present only as $Fe^{III}$ in octahedral and tetrahedral coordination. The magnetic structure is formed by ferromagnetic sheets with the magnetic moments aligned along the *x*-axis and stacked antiferromagnetically perpendicular to the *c*-axis. The electrical properties have been characterized by impedance spectroscopy and reveal both compounds behave as leaky insulators at room temperature with bulk permittivity values $< 20$.

## Introduction

The wide variety of arrangements of corner/face sharing octahedral building blocks in $ABO_3$ perovskite-like compounds is an excellent example of the diversity and flexibility of perovskite-based crystal structures. The 3C- and 2H-$ABO_3$ structural types represent the two "extreme" polytypes of the perovskite structure. The first one is based only on cubic close packed (...ccp...) $AO_3$ layers. The structure consists of a 3D array of corner sharing $BO_6$ octahedra. This structure is stable if the structural tolerance factor *t* is close to one ($t = d_{A-O}/(2^{1/2}d_{B-O})$ where $d_{A-O}$ and $d_{B-O}$ represent the average cation−oxygen interatomic distances of the A- and B-sites, respectively). In contrast, the unit cell of the 2H-type consists of two $AO_3$ layers in a hexagonal close packed (...hcp...) sequence, producing a structure formed by 1D chains of face-sharing $BO_6$ octahedra parallel to the *c*-axis. This structural variety is stabilized for high *t* values ($t > 1$). Between these two extremes, numerous intermediate structures are known to exist, with different degrees of cubic (c) and hexagonal (h) layers, showing a clear example of polytypism.

In $BaM_{1-x}M'_xO_{3-\delta}$ systems (M,M′ = transition metals), the large size of the $Ba^{2+}$ ion favors the presence of h-stacked layers and, depending on both the chemical nature of the M/M′ cations and the oxygen content, several polytypes are stabilized. $BaMnO_3$ adopts the 2H-type structure.[1] The introduction of oxygen vacancies gives rise to a series of hexagonal polytypes following the sequence 2H (hh)-$BaMnO_3$ → 21R (chhhhhh)$_3$-$BaMnO_{2.92}$[2] → 15R (chhhh)$_3$-$BaMnO_{2.90}$ → 8H (chhh)$_2$−$BaMnO_{2.875}$ → 6H′ (hchhhc)-$BaMnO_{2.83}$ → 10H (chchh)$_2$-$BaMnO_{2.80}$ → 4H (hc)$_2$-$BaMnO_{2.75}$,[3] which reveals the level of c-stacked layers to increase with increasing oxygen loss. By using neutron diffraction data, Hayward et al.,[4] have shown $BaMnO_{3-\delta}$ phases to exhibit a strong preference for the anion vacancies to be located in the h-$BaO_3$ layers.

Several perovskite-related structures with different oxygen contents have also been stabilized in $BaFeO_{3-\delta}$. For $0.07 \leq \delta \leq 0.13$ samples prepared under high oxygen pressure conditions, the 12H-type ...(hhcc)$_3$... structure is obtained;[5] for intermediate oxygen contents, $0.2 \leq \delta \leq 0.35$, the 6H-polytype is stabilized.[6] For more oxygen-deficient samples, this system constitutes an excellent example of how the synthetic route influences the resulting structure type. For example, samples prepared by nitrates in the compositional range $BaFeO_{2.50-2.65}$ give

*Corresponding author. E-mail: mparras@quim.ucm.es. Fax: (34) 91 394 43 52.

(1) Hardy, A. *Acta Crystallogr.* **1962**, *15*, 179.
(2) Parras, M.; González-Calbet, J. M.; Alonso, J.; Vallet-Regí, M. *J. Solid State Chem.* **1994**, *113*, 78.
(3) Negas, T.; Roth, R. S. *J. Solid State Chem.* **1971**, *3*, 323.
(4) Adkin, J. J; Hayward, M. *Chem. Mater.* **2007**, *19*, 755.
(5) Grenier, J. C.; Wattiaux, A.; Pouchard, M.; Hagenmuller, P. Parras, M.; Vallet-Regí, M.; González-Calbet, J. M.; Alario-Franco, M. A. *J. Solid State Chem.* **1989**, *80*, 6.
(6) Jacobson, A. J. *Acta Crystallogr. B* **1976**, *32*, 1087.

 Published on Web 10/07/2009 

rise to different crystallographic forms based on c-type stacking of $BaO_{3-\delta}$ layers.[7] When prepared by thermal decomposition of metallo-organic precursors, however, only a 10H polytype is found in the entire composition range $BaFeO_{2.60-2.80}$.[8]

We have recently investigated polytypism in the oxygen-deficient $BaMn_{1-x}Fe_xO_{3-\delta}$ system. A detailed structural characterization of an Fe-rich composition, 10H-$BaMn_{0.4}Fe_{0.6}O_{2.73}$,[9,10] showed that although the basic structure is similar to that of 10H-$BaFeO_{3-\delta}$,[8] differences involving both the crystal structure and anionic vacancy distribution are present in the mixed Mn/Fe phase. Besides, the structural characterization of the $BaMn_{1-x}Fe_xO_{3-\delta}$ ($0 < \delta < 0.3$) system has previously been investigated by V. Caignaert et al.[11] In their study, they stated that the 6H′(hchhhc) polytype is adopted for this compositional range; however, the physical properties were not reported.

In this paper we report a more detailed study of the structural chemistry of two new Mn-rich 6H′ phases within the $BaMn_{1-x}Fe_xO_{3-\delta}$ system: $BaMn_{0.85}Fe_{0.15}O_{2.87}$ and $BaMn_{0.6}Fe_{0.4}O_{2.72}$. In addition, we report the magnetic and electrical properties of these compounds as there has been considerable interest in the physical properties of hexagonal perovskites in recent years. For example, 12R-type $BaMn_{1/2}Ti_{1/2}O_3$[12] and Mn-doped 6H-type $BaTiO_3$[13,14] exhibit high relative permittivity ($\varepsilon_r > 35$) and dielectric resonance at microwave frequencies, thus demonstrating the potential of these materials for applications such as microwave dielectric resonators and/or filters.

## Experimental Section

$BaMn_{0.85}Fe_{0.15}O_{3-\delta}$ ($x = 0.15$) was prepared by conventional solid state reaction from $BaCO_3$ (Aldrich, 99.98%), $MnCO_3$ (Aldrich, 99%) and $Fe_2O_3$ (Aldrich, 99.98%). A well-ground stoichiometric mixture of these reactants was decarbonated in a muffle furnace at 1253 K for 24 h, reground, and then heated in a Pt crucible at 1573 K in air for 5 days with intermediate grinding each 24 h. The same process was repeated at 1598 and 1623 K; finally the powder was heated at 1648 K for 12 h, and then quenched to room temperature in air.

$BaMn_{0.6}Fe_{0.4}O_{3-\delta}$ ($x = 0.40$) was prepared by a wet chemical method. The starting materials were $BaCO_3$ (Aldrich, 99.98%), $MnCO_3$ (Aldrich, 99%) and $Fe(NO_3)_3 \cdot 9H_2O$. Because of the hygroscopic nature of $Fe(NO_3)_3 \cdot 9H_2O$, a thermogravimetrical analysis was carried out to establish the nominal composition of this reactant. It was determined to be $Fe(NO_3)_3 \cdot 9.38H_2O$. A stoichiometric mixture of the above reactants was dissolved in ~80 mL of hot aqueous acid ($HNO_3$) solution, which was slowly heated to evaporate the solvent. This so-obtained solid was dried and then transferred to an $Al_2O_3$ plate-like crucible and calcined at 973 K for 72 h. This powder was heated in a Pt crucible at 1373 K for 96 h, 1423 K for 48 h, and 1473 K for 144 h, with intermediate grindings each 48 h. Finally, the sample was quenched at room temperature in air.

The average cation composition of the powder was determined by inductive coupling plasma (ICP), whereas the local composition was analyzed by energy-dispersive X-ray spectroscopy (EDS) with an INCA analyzer system attached to a JEOL 3000 FEG electron microscope.

Powder X-ray diffraction (XRD) patterns were collected using Cu Kα monochromatic radiation ($\lambda = 1.54056$ Å) at room temperature on a Panalytical X′PERT PRO MPD diffractometer equipped with a germanium 111 primary beam monochromator and X'Celerator fast detector. Neutron powder diffraction (NPD) data were collected at room temperature on the high resolution two-axis powder diffractometer D1A at the Institute Laue Langevin (ILL), Grenoble (France) with neutrons of wavelength 1.908 Å. The angular range covered by the detectors extends from −10° to 160° with a step size of 0.05°. Neutron diffraction data were collected from samples at different temperatures on the high flux D1B instrument. Diffraction data were analyzed by the Rietveld method[15] using the Fullprof program.[16]

Selected area electron diffraction (SAED) and high resolution electron microscopy (HREM) were performed using a JEOL 3000 FEG electron microscope, fitted with a double tilting goniometer stage (±22°, ±22°). Simulated HREM images were calculated by the multislice method using the MacTempas software package.

Mössbauer spectroscopy was performed with a constant acceleration Halder-type spectrometer using a room temperature $^{57}Co$ source (Rh matrix) in transmission geometry. The polycrystalline absorbers containing about 10 mg/cm$^2$ of iron were used to avoid the experimental widening of the peaks. The velocity was calibrated using pure iron metal as the standard material. The spectra were recorded at 4.2 and 293 K. First, the spectra were fitted to Lorentzian lines, allowing the position, amplitude, and width of each line to be refined. The experimental hyperfine parameters of the different iron sites were deduced from this first approach. In a second stage, calculations by the method of Hesse and Rubartsch[17] were performed to deconvolute the spectra in terms of the distribution of the hyperfine parameters. This method is often used for disordered compounds that are characterized by a broad distribution of possible environments, leading to experimental spectra with lines of significant width and profiles that deviate from a Lorentzian fit. Isomer shifts are expressed with respect to α-iron at 293 K.

DC magnetization was measured in a SQUID magnetometer, in the range ~2 to 300 K under an applied magnetic field of 1000 Oe. The field dependence of the magnetization at 2 K was carried out in the range 0−50 kOe.

Powder was milled using a mortar and pestle and uniaxially pressed (Specac, Kent, UK) into cylindrical (length ≈ 5 mm) pellets under an applied pressure of 50 MPa and then

(7) González-Calbet, J. M.; Parras, M.; Vallet-Regí, M.; Grenier, J. C. *J. Solid State Chem.* **1990**, *86*, 149.
(8) Delattre, J. L; Stacy, A. M.; Siegrist, T. *J. Solid State Chem.* **2004**, *177*, 928.
(9) Miranda, L.; Ramírez-Castellanos, J.; Hernando, M.; Varela, A.; González-Calbet, J. M.; Parras, M. *Eur. J. Inorg. Chem.* **2007**, 2129.
(10) Miranda, L.; Boulahya, K.; Varela, A.; González-Calbet, J. M.; Parras, M.; Hernando, M.; Fernández-Díaz, M. T.; Feteira, A.; Sinclair, D. C. *Chem. Mater.* **2007**, *19*, 3425.
(11) Caignaert, V.; Hervieu, M.; Domengès, B.; Nguyen, N.; Pannetier, J.; Raveau, B. *J. Solid State Chem.* **1988**, *73*, 104.
(12) Keith, G. M.; Kirk, C. A.; Sarma, K.; Alford, N.; Cussen, E. J.; Rosseinsky, M. J.; Sinclair, D. C. *Chem. Mater.* **2004**, *16*, 2007.
(13) Keith, G. M.; Sarma, K.; Alford, N. M.; Sinclair, D. C. *J. Electroceram.* **2004**, *13*, 305.
(14) Miranda, L.; Feteira, A.; Sinclair, D. C.; Boulahya, K.; Hernando, M.; Ramírez, J.; Varela, A.; González-Calbet, J. M.; Parras, M. *Chem. Mater.* **2009**, *21*, 1731.
(15) Rietveld, H. M. *J. Appl. Crystallogr.* **1969**, *2*, 65.
(16) Rodríguez- Carvajal, J. *J. Phys. B* **1993**, *192*, 55.
(17) Hesse, J.; Rubartsch, A. *J. Phys. E. Sci. Instrum.* **1974**, *7*, 526.

isostatically pressed (model CIP 32330, Flow Autoclave System Inc., Columbus, OH) at 200 MPa. Pellets were sintered in air at 1648 K ($x = 0.15$) and 1473 K ($x = 0.40$) for 2 h and then quenched to room temperature. The ceramic density was 5.58 $g \cdot cm^{-3}$ (93% of the theoretical X-ray density) and 4.35 $g \cdot cm^{-3}$ (75% of the theoretical density), for $BaMn_{0.85}Fe_{0.15}O_{2.87}$ and $BaMn_{0.6}Fe_{0.4}O_{2.72}$, respectively. Electrodes fabricated from gold paste (T-10112, Engelhard-CLAL, Cinderford, Gloucestershire, UK) were applied to both major faces of the pellets, which were sintered in air at 1073 K for 1 h to remove volatiles and harden the residue. The electrical properties of $BaMn_{0.85}Fe_{0.15}O_{2.87}$ and $BaMn_{0.6}Fe_{0.4}O_{2.72}$ ceramics were investigated in the temperature range 10−300 K using a cryocooler coupled to an LCR bridge (model E4980A, Agilent, Palo Alto, CA) and to an impedance analyzer (model HP 4192A, Hewlett-Packard, Palo Alto, CA) for fixed frequency capacitance and impedance spectroscopy (IS) measurements, respectively. All impedance data were corrected for sample geometry and analyzed using the commercial software package Z-view (Scribner Associates, Inc., Charlottesville, VA, version 2.1).

## Results and Discussion

As pointed out in the Introduction, the preparative method greatly influences the stabilization of a particular polytype for a given composition. According to previous results, the 6H′ type is stable up to $x = 0.3$ for samples prepared by a mixed-oxide, solid state reaction route. However, when prepared from a nitrate solution, the stability range of 6H′ increases to $x = 0.4$.

The cationic composition of the samples, determined on several dozens of small crystallites by EDS analysis in the electron microscope, is in agreement with the nominal one. The oxygen content was obtained from the analysis of the neutron diffraction data and will be discussed below.

The XRD pattern of both compounds can be indexed on the basis of a hexagonal unit cell with $P\bar{6}m2$ space group and cell parameters $a = 5.68354(3)$ Å, $c = 14.31472(10)$ Å, and $a = 5.71707(8)$ Å, $c = 14.3211(2)$ Å, for $x = 0.15$ and 0.40, respectively. The lattice parameters are consistent with a hexagonal 6H′ polytype according to previous results.[11] The layer sequence of the polytype can be directly obtained from a [010] HREM image. Moreover, it is worth mentioning that stacking faults are a common occurrence in polytypic materials and are also easily detected by SAED and HREM. To complete this structural study, both samples were therefore microstructurally characterized by these techniques.

Both samples depicted the same SAED pattern. Figure 1a,b shows those corresponding to $x = 0.15$ along [010] and [1$\bar{1}$0] zone axes, respectively. All reflections are indexed on the basis of a hexagonal unit cell with lattice parameters close to $a = 5.68$ and $c = 14.31$ Å. The observed reflection spots on the SAED pattern along [1$\bar{1}$0] are in agreement with the $P\bar{6}m2$ space group, as expected for the 6H′ (...hchhhc...) polytype. All diffraction spots appear sharp and without any apparent streaking along the $c^*$ axis.

Figure 2 corresponds to the most informative HREM image and simulation taken along the [010] direction

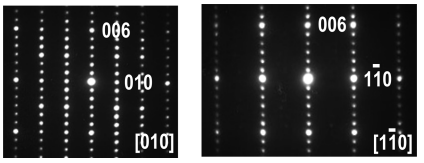


**Figure 1.** SAED pattern along zone axes (a) [010] and (b) [1$\bar{1}$0] corresponding to $BaMn_{0.85}Fe_{0.15}O_{2.87}$.

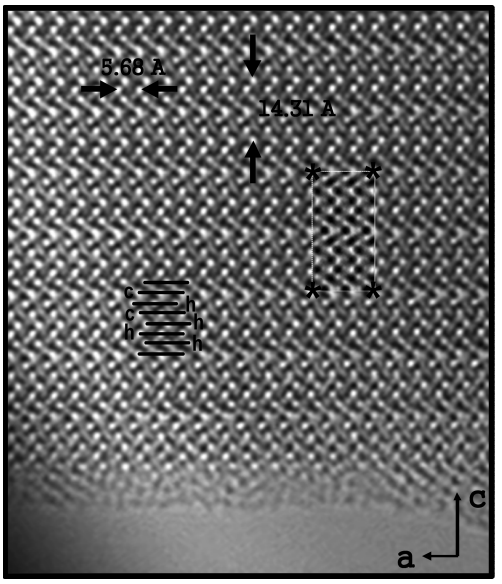


**Figure 2.** [010] HREM image corresponding to $BaMn_{0.85}Fe_{0.15}O_{2.87}$. The simulation image can be observed at the inset.

of $x = 0.15$. In this zone, the structure is viewed parallel to the columns of Ba−O close packed rows and the stacking sequence of the layers is revealed directly. According to this, the observed contrast of the image can be interpreted as corresponding to a (...hchhhc...) layer arrangement. The simulation of the image, inset of Figure 2, fits perfectly with the experimental one for $\Delta f = -5$ nm and $\Delta t = 5$ nm. The sequence is extended over the whole crystal; therefore, the presence of any significant intergrowth can be discarded.

To get additional information regarding the cationic distribution of Fe and Mn over the three available crystallographic positions, as well as the arrangement of the anionic vacancies, a neutron diffraction study was performed. The large contrast between the scattering lengths of Mn (−3.750 fm) and Fe (9.45 fm) makes neutron diffraction a suitable tool for this purpose. The NPD data collected at room temperature were refined using the structural parameters of 6H′-$BaMnO_{3-\delta}$[3] polytype as a starting model. This structure is formed by blocks of four face sharing octahedral ($M_4O_{15}$) units linked by corners to blocks of two face sharing octahedral ($M_2O_9$) units.

The atomic coordinates, isotropic thermal parameters, and occupancy factors of all atoms were refined. Initially, the Mn:Fe ratio on the three available sites were also refined. All sites were constrained to be fully occupied but no constraint was imposed on the Mn:Fe ratio. The occupancy factors of the oxygen atoms reveal the anionic sublattice is not complete; the full composition obtained

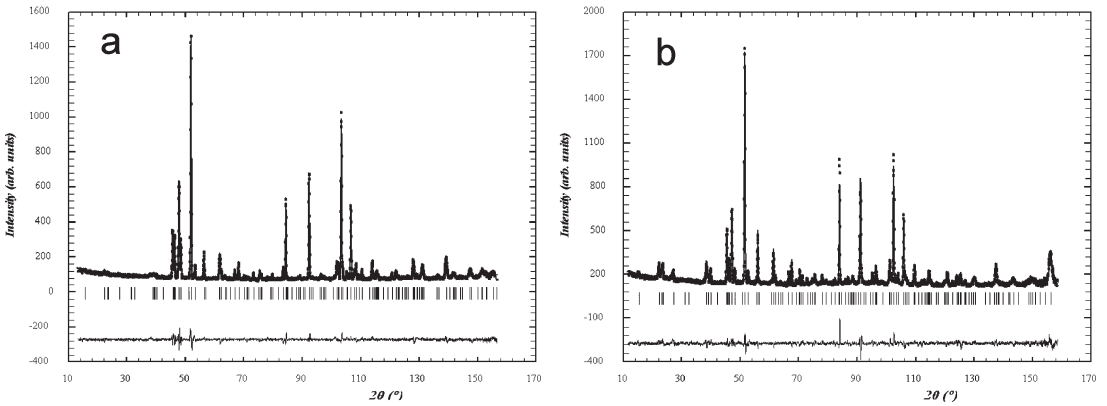


**Figure 3.** Observed, calculated, and difference profile of neutron diffraction patterns for (a) $BaMn_{0.85}Fe_{0.15}O_{2.87}$ and (b) $BaMn_{0.60}Fe_{0.40}O_{2.72}$ at room temperature.

for both compounds was $BaMn_{0.85}Fe_{0.15}O_{2.87}$ and $BaMn_{0.60}Fe_{0.40}O_{2.72}$.

The Rietveld refinement pattern and difference plot for $BaMn_{0.85}Fe_{0.15}O_{2.87}$ and $BaMn_{0.60}Fe_{0.40}O_{2.72}$ are shown in Figure 3 panels a and b, respectively. The obtained structural parameters are listed in Table 1 and selected interatomic distances for both compounds are given in Table 2.

A schematic representation of the structure is depicted in Figure 4. It is formed by tetramers and dimers of face-sharing octahedra that are linked by corners. The distribution of Mn and Fe over the different polyhedra is summarized in Table 1. In both phases, the M2 site (center of the tetramers) is fully occupied by Mn. The remaining Mn and Fe cations are randomly distributed over the two crystallographically distinct sites, M1 and M3, corresponding to the outer octahedra of the tetramer and dimer, respectively. These results reflect the strong tendency of $Mn^{4+}$ to occupy face-sharing octahedra as observed in 12H-$BaMn_{0.4}Co_{0.6}O_{2.83}$,[18] 5H-$BaMn_{0.2}Co_{0.8}O_{2.8}$[19] and 10H-$BaMn_{0.4}Fe_{0.6}O_{2.73}$.[10] On the other hand, Fe ions are preferentially located at the outer sharing corner octahedra as in 10H-$BaMn_{0.4}Fe_{0.6}O_{2.73}$,[10] $Ba_5Fe_4NiO_{13.5}$,[20] and $BaMn_{0.766}Fe_{0.233}O_{2.87}$.[11]

The inner octahedra of the tetramer (M2) are nearly regular (see distances in table 2). The M2−O distances are in excellent agreement with that observed for Mn−O in the same oxygen environment for $BaMnO_{3-\delta}$ related structures: 1.9044 Å in 2H-$BaMnO_3$,[20] 1.8999 Å in 15R-$BaMnO_{2.99}$,[4] 1.8959 Å in 10H-$BaMnO_{2.91}$,[4] and 1.903−1.893 Å in 6H′-$BaMnO_{2.92}$.[4] The outer octahedra, of the tetramer (M1) and the octahedra associated with the M3 site are distorted with different M−O distances, see Table 2. This displacement of the metal atoms (Mn, Fe) from the center toward the fully occupied oxygen sites of the cubic layer reduces electrostatic repulsion between cations in adjacent face-sharing octahedra, leading to an increase of the metal−metal separation in the dimers (M3−M3) and in the outer octahedra of the tetramers (M2−M1) with respect to M2−M2. This feature has been observed in other hexagonal polytypes, including 12H-$BaMn_{0.4}Co_{0.6}O_{2.83}$[18] and 12R-$BaMn_{0.5}Ti_{0.5}O_3$.[12] The (M3, M1)−O distances in $BaMn_{0.85}Fe_{0.15}O_{2.87}$ and $BaMn_{0.6}Fe_{0.4}O_{2.72}$ are very similar to those (Fe, Mn)−O in the terminal octahedron of 10H-$BaMn_{0.4}Fe_{0.6}O_{2.73}$ (2.060, 1.893 Å),[10] 6H′-$BaMn_{0.766}Fe_{0.233}O_{2.87}$,[11] and other similar compounds.[6,8,20]

The refinement of the oxygen occupancies (Table 1) shows the presence of anionic vacancies in both compounds. The anionic deficiency increases with Fe-content. These anionic vacancies are randomly distributed in the hexagonal layers, in particular in the Ba4−O4 and Ba1−O2 layers. The anionic composition for each layer is also given in Table 1. The high oxygen vacancy concentration corresponds to the hexagonal $Ba(1)O(2)_{2.484}$ and $Ba(1)O(2)_{1.588}$ layers in the $M_2O_9$ structural block for $BaMn_{0.85}Fe_{0.15}O_{2.87}$ and $BaMn_{0.6}Fe_{0.4}O_{2.72}$, respectively. These results agree with that given for $BaMn_{0.766}Fe_{0.233}O_{2.87}$[11] where anionic vacancies were located in the same hexagonal layers. However, the lower concentration of vacancies (close to 4%) found in our samples at the Ba4−O4 layers in the $M_4O_{15}$ units are not detected in $BaMn_{0.766}Fe_{0.233}O_{2.87}$,[11] probably due to the low resolution of the D1B instrument used for the collection of neutron diffraction data.

According to Adkin et al.[4] this preferential location for oxygen-deficiency in a given layer can be rationalized by examining the different coordination environments adopted by oxide ions in the structures, particularly the barium−oxygen bonds, in such a way that the longest distances indicate the weakest bonding interactions. To remove these oxide ions seems to be the most favorable process. In a 6H′-polytype, there are four different environments for the oxide ions: the central layer of a ...hhh... (A), ...chc... (B), ...hch... (C), or a ...chh... (D) stacking sequence (Figure 4). The calculated average distances reveal the largest Ba−O distances correspond to the oxide ions within the h-stacked layer in the chc-unit ($M_2O_{9-\delta}$ structure block) which corresponds to the preferential site where the oxygen vacancies are located. On the other hand, although average Ba−O distances in both ...hhh... (A) and

(18) Miranda, L.; Ramírez-Castellanos, J.; Varela, A.; González-Calbet, J. M.; Parras, M.; Hernando, M.; Fernández-Díaz, M. T.; García-Hernández, M. *Chem. Mater.* **2007**, *19*, 1503.
(19) Miranda, L.; Feteira, A.; Sinclair, D. C.; García Hernández, M.; Boulahya, K.; Hernando, M.; Varela, A.; González-Calbet, J. M.; Parras, M. *Chem. Mater.* **2008**, *20*, 2818.
(20) Takizawa, H.; Steinfink, H. *J. Solid State Chem.* **1996**, *121*, 133.

**Table 1. Structural Parameters from the Refinement for $BaMn_{0.85}Fe_{0.15}O_{2.87}$ and $BaMn_{0.6}Fe_{0.4}O_{2.72}$[a]**

| | $BaMn_{0.85}Fe_{0.15}O_{2.87}$ | $BaMn_{0.6}Fe_{0.4}O_{2.72}$ |
|---|---|---|
| Ba1 (0, 0, 0) | | |
| Biso (Å$^2$) | 0.36(18) | 0.62088 |
| Occ | 1 | 1 |
| Ba2 ($^1/_3$, $^2/_3$, 0.5) | | |
| Biso (Å$^2$) | 0.7(3) | 0.4647 |
| Occ | 1 | 1 |
| Ba3 ($^1/_3$, $^2/_3$, *z*) | | |
| *z* | 0.1783(4) | 0.1938(4) |
| Biso (Å$^2$) | 0.31(14) | 038544 |
| Occ | 1 | 1 |
| Ba4 ($^1/_3$, $^2/_3$, *z*) | | |
| *z* | 0.3391(3) | 0.3459(5) |
| Biso(Å$^2$) | 0.8(2) | 1.20719 |
| Occ | 1 | 1 |
| M1 (0, 0, *z*) | | |
| *z* | 0.2435(2) | 0.2432(2) |
| Biso (Å$^2$) | 0.4(2) | 1.12385 |
| Occ | 0.941(2)/0.059(2)[b] | 0.646(6)/0.353(6)[b] |
| M2 (0, 0, *z*) | | |
| *z* | 0.4170(1) | 0.4178(3) |
| Biso (Å$^2$) | 0.53(16) | 1.25245 |
| Occ | 1/0[b] | 1/0[b] |
| M3 ($^2/_3$, $^1/_3$, *z*) | | |
| *z* | 0.1133(2) | 0.1131(3) |
| Biso (Å$^2$) | 0.5(4) | 1.92605 |
| Occ | 0.612(3)/0.387(3)[b] | 0.210(6)/0.790(1)[b] |
| O1 (*x*, 2*x*, 0.5) | | |
| *x* | 0.8475(12) | 0.8472(12) |
| Biso (Å$^2$) | 0.24(14) | 0.29597 |
| Occ | 1⟹$BaO_3$ | 1⟹$BaO_3$ |
| O2 (*x*, 2*x*, 0) | | |
| *x* | 0.5167(17) | 0.521(2) |
| Biso (Å$^2$) | 1.99(12) | 2.17099 |
| Occ | 0.828⟹$BaO_{2.484}$ | 0.529(12) ⟹$BaO_{1.588}$ |
| O3 (*x*, 2*x*, *z*) | | |
| *x* | 0.8328(9) | 0.8371(8) |
| *z* | 0.1637(5) | 0.1642(4) |
| Biso (Å$^2$) | 0.93(9) | 1.15304 |
| Occ | 1⟹$BaO_3$ | 1⟹ $BaO_3$ |
| O4 (*x*, 2*x*, *z*) | | |
| *x* | 0.1468(9) | 0.1493(10) |
| *z* | 0.32942(19) | 0.3312(2) |
| Biso (Å$^2$) | 0.38(11) | 0.73(2) |
| Occ | 0.962(16) ⟹$BaO_{2.886}$ | 0.958(12) ⟹$BaO_{2.876}$ |
| *a*, *b* (Å) | 5.68713(7) | 5.71087(9) |
| *c* (Å) | 14.311051(2) | 14.3173(3) |

[a] Space group $P\bar{6}m2$ (No. 187). Fit parameters for $BaMn_{0.85}Fe_{0.15}O_{2.87}$: $R_F$ = 3.96, $R_{exp}$ = 3.60, $R_B$ = 5.46, $\chi^2$ = 2.24. For $BaMn_{0.6}Fe_{0.4}O_{2.72}$: $R_F$ = 4.52, $R_{exp}$ = 3.58, $R_B$ = 6.80, $\chi^2$ = 2.55. [b] Mn/Fe.

...chh... (D) blocks are similar, the small remaining level of anionic vacancies (4%) is located only in the chh-block. This fact can be related to the enhancement of electrostatic repulsions between M cations surrounded by an oxygen-deficient layer. To minimize these repulsions, the metal atoms are displaced away from the center toward the adjacent cubic layers, thus stabilizing the structure.

Regarding the accommodation of oxygen vacancies in anionic deficient hexagonal perovskites, significant differences can be stated as a function, among other factors, of the chemical nature of the transition metal. For instance, in $BaCoO_{3-\delta}$,[22] the arrangement of oxygen

**Table 2. Selected Interatomic Distances (Å) in $BaMn_{0.85}Fe_{0.15}O_{2.87}$ and $BaMn_{0.6}Fe_{0.4}O_{2.72}$**

| | $BaMn_{0.85}Fe_{0.15}O_{2.87}$ | $BaMn_{0.6}Fe_{0.4}O_{2.72}$ |
|---|---|---|
| Ba1−O2 | 2.8480(12) ×3 | 2.861(18) ×3 |
| −O2 | 2.848(7) ×3 | 2.860(12) ×3 |
| −O3 | 2.835(3) ×6 | 2.851(5) ×6 |
| Ba2−O1 | 2.845(4) ×6 | 2.859(8) ×6 |
| −O4 | 3.006(3) ×6 | 3.025(3) ×6 |
| Ba3−O2 | 3.133(8) | 3.341(10) ×3 |
| −O3 | 2.851(6) ×6 | 2.887(6) ×6 |
| −O4 | 2.811(6) ×3 | 2.680(6) ×3 |
| Ba4−O1 | 2.938(5) ×3 | 2.839(7) |
| −O3 | 2.912(5) ×3 | 3.099(9) |
| −O4 | 2.849(3) ×6 | 2.868(4) |
| M1−O3 | 1.993(5) ×3 | 1.967(4) |
| −O4 | 1.883(3) ×3 | 1.941(4) |
| M2−O1 | 1.903(4) ×3 | 1.914(5) |
| −O4 | 1.898(3) ×3 | 1.929(4) |
| M3−O2 | 2.175(6) ×3 | 2.165(11) |
| −O3 | 1.783(4) ×3 | 1.839(5) |
| M1−M2 | 2.477(2) | 2.501(3) |
| M2−M2 | 2.342(1) | 2.351(3) |
| M3−M3 | 3.197(3) | 3.241(2) |

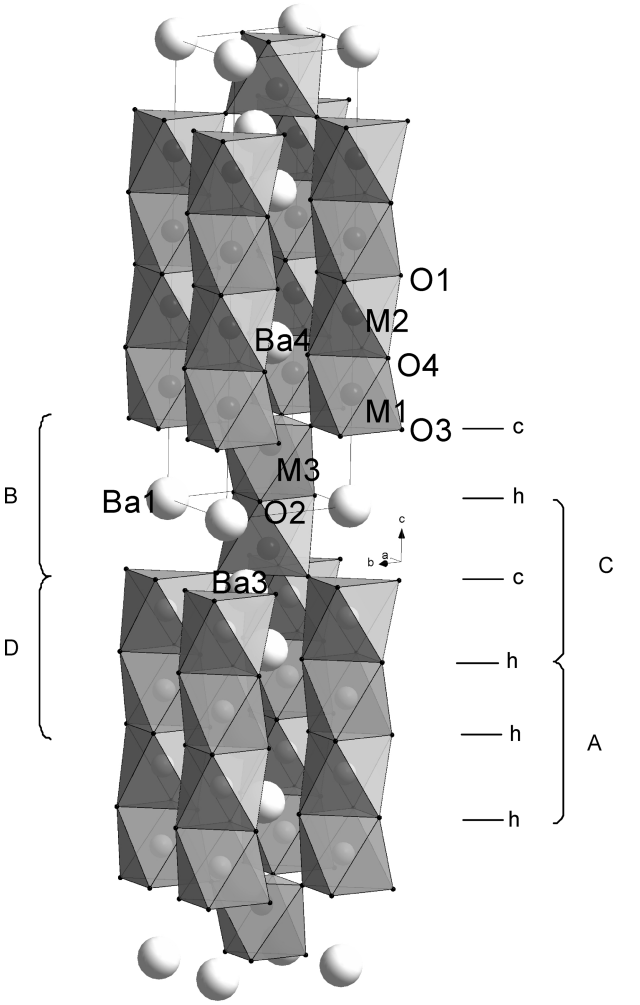


**Figure 4.** Structural model for 6H′-$BaMn_{1-x}Fe_xO_{3-y}$ ($x$ = 0.15 and 0.60).

(21) Cussen, E. J.; Battle, P. D. *Chem. Mater.* **2000**, *12*, 831.
(22) Boulahya, K.; Parras, M.; González-Calbet, J. M.; Amador, U.; Martínez, J. L; Tissen, V.; Fernández-Díaz, M. T. *Phys. Rev. B* **2005**, *71*, 144402.

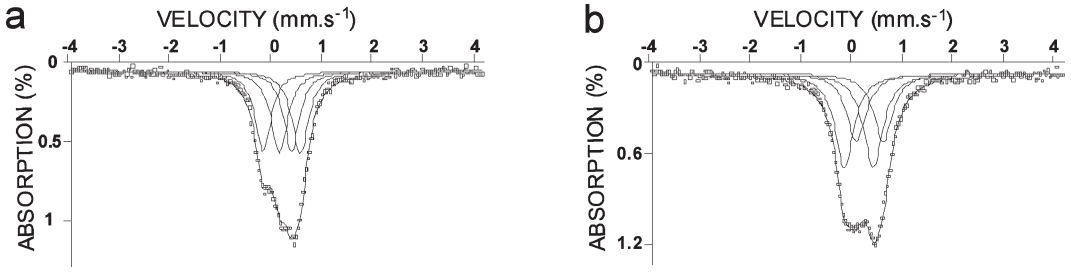


**Figure 5.** Mössbauer spectra corresponding to (a) $BaMn_{0.85}Fe_{0.15}O_{2.87}$ and (b) $BaMn_{0.60}Fe_{0.40}O_{2.72}$ at room temperature.

vacancies in cubic $BaO_2$ layers gives rise to new ordered phases with Co in both tetrahedral and octahedral environments. Moreover, in this system, a particular ordered polytype is only stable for a given anionic composition in such a way that variations in the oxygen content gives rise to a phase mixture of the closest polytypes. The same behavior is observed in $BaMn_{1-x}Co_xO_{3-\delta}$.[18,19]

On the contrary, in 6H-$BaTiO_{3-\delta}$,[23] 6H-$BaFeO_{3-\delta}$,[6] and 4H-$BaMnO_{3-\delta}$,[24] a given polytype is stable in an oxygen compositional range ($0 \le \delta \le 0.15$ for Ti, $0.01 \le \delta \le 0.35$ for Fe, and $0 \le \delta \le 0.35$ for Mn). Besides, the oxygen vacancies are located only in the hexagonal layers. This seems to be the general case for many hexagonal perovskites with a random distribution of anionic vacancies. Neutron diffraction results show the 6H′-$BaMn_{0.85}Fe_{0.15}O_{2.87}$ and 6H′-$BaMn_{0.6}Fe_{0.4}O_{2.72}$ studied here to behave in the same manner as the above-mentioned 6H-type systems with the oxygen vacancies located randomly only in the hexagonal layers.

To get information about both oxidation state and oxygen environment of Fe, we have carried out a Mössbauer spectroscopy study. Figure 5 shows the Mössbauer spectra corresponding to $BaMn_{0.85}Fe_{0.15}O_{2.87}$ (a) and $BaMn_{0.60}Fe_{0.40}O_{2.72}$ (b) at room temperature. Both spectra can be described in terms of two quadrupolar doublets indicating that iron ions are distributed over two different crystallographic sites. The calculation using distributions of the hyperfine parameters is justified by the nonordered nature of the crystal structure giving rise to chemical disorder around the iron ions. Mössbauer spectroscopy parameters for both compounds are summarized in Table 3. It is worth mentioning that, even if not detected by XRD, the presence of some traces of $Fe_2O_3$ (less than 1%) cannot be disregarded in the spectrum of the iron-rich composition, $BaMn_{0.6}Fe_{0.4}O_{2.72}$ (Figure 5 b). The Γ value, ($\approx$ 0.40 mm/s), is slightly high, probably due to some disorder around Fe, according to the structural study which shows some cationic disorder and vacancies around iron. The isomer shift value corresponding to the first distribution (0.39 mm/s) suggests trivalent iron in octahedral coordination. On the contrary, the weak value (0.15−0.16 mm/s) corresponding to the second distribution indicates a more covalent environment with shorter Fe−O distances. These values are characteristic of iron in 4-fold coordination.

**Table 3. Summary of Mössbauer Spectroscopy Data at 293 K**

| | δ (mm/s) | Δ (mm/s) | Γ (mm/s) | % | site |
|---|---|---|---|---|---|
| $BaMn_{0.85}Fe_{0.15}O_{2.87}$ | 0.39(2) | 0.42(2) | 0.40(1) | 52 | $Fe^{3+}$ [$O_h$] |
| | 0.15(2) | 0.57(2) | 0.38(1) | 48 | $Fe^{3+}$ [$T_d$] |
| $BaMn_{0.60}Fe_{0.40}O_{2.72}$ | 0.37(4) | 0.46(2) | 0.45(2) | 42 | $Fe^{3+}$ [$O_h$] |
| | 0.16(3) | 0.57(3) | 0.46(2) | 58 | $Fe^{3+}$ [$T_d$] |

Mössbauer spectra corresponding to $BaMn_{0.85}Fe_{0.15}O_{2.87}$ and $BaMn_{0.60}Fe_{0.40}O_{2.72}$ at 4.2 K show magnetic order as depicted in Figure 6a,b, respectively. Results of the calculated spectra are shown in Table 4. Both spectra can be fitted by using two magnetic sextets describing two ordered magnetic sites. Hyperfine parameters (δ, **H**), in agreement with room temperature data, are consistent with two crystallographic sites for trivalent iron: actually, δ (0.45 mm/s) and **H** (∼45 T) are values characteristic of iron in 6-fold coordination whereas δ (∼0.29 mm/s) and **H** (∼38 T) can be fitted to iron in 4-fold coordination. The difference between δ data obtained at room temperature and 4.2 K are due to the second order Doppler effect.

Mössbauer spectroscopy results indicate that iron is present only in the trivalent state in both compounds and is located in two different oxygen environments, octahedral and tetrahedral, in a ratio close to 50:50%. According to the anionic content of both compositions, Mn ions must be present in III and IV oxidation states according to the following chemical compositions: $BaMn^{IV}_{0.74}Mn^{III}_{0.11}Fe^{III}_{0.15}O_{2.87}$ and $BaMn^{IV}_{0.44}Mn^{III}_{0.17}Fe^{III}_{0.39}O_{2.72}$. $Fe^{III}$ is frequently found in both octahedral and tetrahedral sites, for example in the inverse spinel $Fe_3O_4$,[25] whereas Mn adopts octahedral ($Mn^{4+}$) or V-fold coordination ($Mn^{3+}$) according to the oxidation state. The vacancy content in the h-layers in the chc-block ($M_2O_9$ dimers) can therefore be interpreted in terms of edge-sharing pairs of square pyramids containing $Mn^{III}$ and corner-sharing pairs of tetrahedra for $Fe^{III}$ cations. $FeO_4$ tetrahedra result from the creation of two oxygen vacancies out of the three oxygen sites from the two face-sharing octahedra, whereas the $MnO_5$ pyramids correspond to the creation of one vacancy out of the three. According to the Mössbauer spectroscopy and neutron diffraction results we propose the M2 site, with nearly regular octahedral coordination, will be completely occupied by $Mn^{IV}$ (Mn−O distances very close to that found in $BaMnO_3$[21]), whereas $Mn^{3+}$, with an associated Jahn−Teller effect, occupies the most distorted and oxygen-deficient sites, M1 and M3 sites, with pyramidal

(23) Sinclair, D. C.; Skakle, J. M. S.; Morrison, F. D.; Smith, R. I.; Beales, T. P. *J. Mater. Chem.* **1999**, *9*, 1327.
(24) Adkin, J. J.; Hayward, M. A. *J. Solid State Chem.* **2006**, *179*, 70.
(25) Fleet, M. E. *Acta Crystallogr. B* **1981**, *37*, 917.

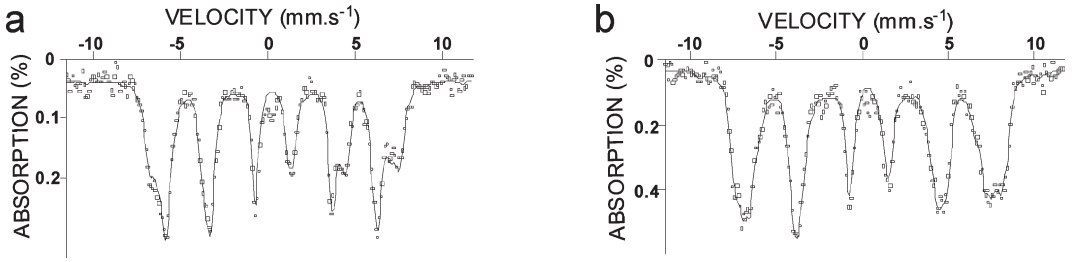


**Figure 6.** Mössbauer spectra corresponding to (a) $BaMn_{0.85}Fe_{0.15}O_{2.87}$ and (b) $BaMn_{0.60}Fe_{0.40}O_{2.72}$ at 4 K.

**Table 4. Summary of Mössbauer Spectroscopy Data at 4.2 K**

| | $\delta$ (mm/s) | $\Gamma$ (mm/s) | $\varepsilon$ (mm/s) | **H** (T) | % | site |
|---|---|---|---|---|---|---|
| $BaMn_{0.85}Fe_{0.15}O_{2.87}$ | 0.46 | 0.35 | −0.001 | 43 | 52 | $Fe^{3+}$ [$O_h$] |
| | 0.28 | 0.40 | 0.001 | 36 | 48 | $Fe^{3+}$ [$T_d$] |
| $BaMn_{0.60}Fe_{0.40}O_{2.72}$ | 0.46 | 0.45 | −0.001 | 46 | 48 | $Fe^{3+}$ [$O_h$] |
| | 0.30 | 0.50 | 0.001 | 39 | 52 | $Fe^{3+}$ [$T_d$] |

coordination in both samples. Regarding Fe atoms, they will be in octahedral coordination in the M1 sites; in the $M_2O_9$ units, M3 sites, the Fe cations should be located in both tetrahedral and octahedral coordination in good agreement with the anionic stoichiometry of the oxygen deficient hexagonal layers. The coexistence of distinct oxygen polyhedra around the M3 metallic position gives rise to a disordered distribution of the anionic vacancies in the hexagonal layers as reflected in the temperature factors (see Table 1).

The Mn/Fe cationic distribution reflects the strong preference of $Mn^{4+}$ to occupy face-sharing octahedra and the preference of Fe to be located at corner sharing octahedra. However, a fully cationic ordered array is not attained. A large difference in cation size and/or charge has been reported to provide suitable enthalpic drive to form cation ordered structures. This strategy has been successfully used to stabilize several hexagonal perovskites with an ordered cationic distribution. For example, the different size and charge of Cr(V), Mn(II), and Mn(IV) in $Ba_7Mn_5Cr_2O_{20}$[26] lead to a fully ordered structure. Such a situation is not achieved in any of the phases studied here since neither the size and/or charge of Fe(III), Fe(IV), Mn(III), and Mn(IV) are sufficiently different to stabilize structures with cationic order. Moreover, although both Mn(IV) and Fe(III) show a clear preference for different environments (M2 and M3 in Figure 4, respectively), even stabilizing different oxygen coordination sites, the disorder of the anionic vacancies remain up to a relatively large concentration.

## Magnetic Properties

Magnetic susceptibility measurements collected from both samples as a function of the temperature (Figure 7) show a divergence between zero-field-cooled (ZFC) and field-cooled (FC) data, below 280 and 180 K (marked with an arrow in Figure 7) for $BaMn_{0.85}Fe_{0.15}O_{2.87}$ and

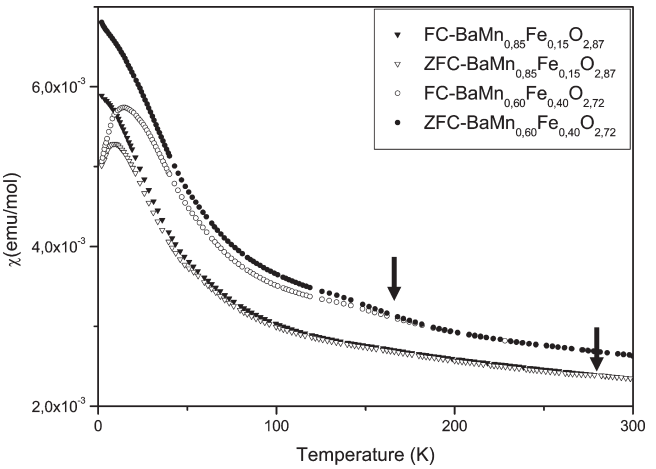


**Figure 7.** ZFC and 1 kOe FC magnetic susceptibility data for $BaMn_{0.85}Fe_{0.15}O_{2.87}$ and $BaMn_{0.60}Fe_{0.40}O_{2.72}$.

$BaMn_{0.60}Fe_{0.40}O_{2.72}$, respectively. In both cases, this divergence may be associated with a magnetic transition. At $T \approx 50$ K, there is a significant increase in the FC data. The samples are not strictly in the Curie−Weiss limit over the measured temperature range; however, the fit of the susceptibility data to the Curie−Weiss law at temperatures close to room temperature shows a negative and large Curie−Weiss temperature ($\theta \approx -750$ K) for both samples, indicating the presence of very strong antiferromagnetic (AFM) interactions. AFM short-range coupling between adjacent atoms in the face-sharing octahedral strings is present in other Mn-based hexagonal perovskites, such as $BaMnO_{3-\delta}$,[21] $SrMnO_3$,[27] and 4H-(BaSr)$MnO_{3-\delta}$[24] and are presumably responsible for the AFM short-range coupling in $x = 0.15$ and 0.40.

The variation of magnetization with a magnetic field at 2 K is shown in Figure 8a,b for both samples, and a hysteresis loop can be observed (discussed later). To get additional information about the magnetic features of these phases, variable temperature neutron diffraction data were collected on the high flux instrument D1B.

Extra intensity not accounted for by the structural model was evident in the (003) at $2\theta \approx 31°$, (103) at $2\theta \approx 36°$ and (102) at $2\theta \approx 43°$ reflections, for $BaMn_{0.85}Fe_{0.15}O_{2.87}$ and $BaMn_{0.60}Fe_{0.40}O_{2.72}$ at temperature below 275 and 175 K, respectively (see inset in Figure 9). These contributions to the diffraction pattern were analyzed by considering that they were magnetic in

(26) Dunstone, S. J.; Clark, J. H.; Hayward, M. A. *Chem. Commun.* **2007**, *19*, 1905.

(27) Battle, P. D.; Gibb, T. C.; Jones, C. W. *J. Solid State Chem.* **1988**, *74*, 60.

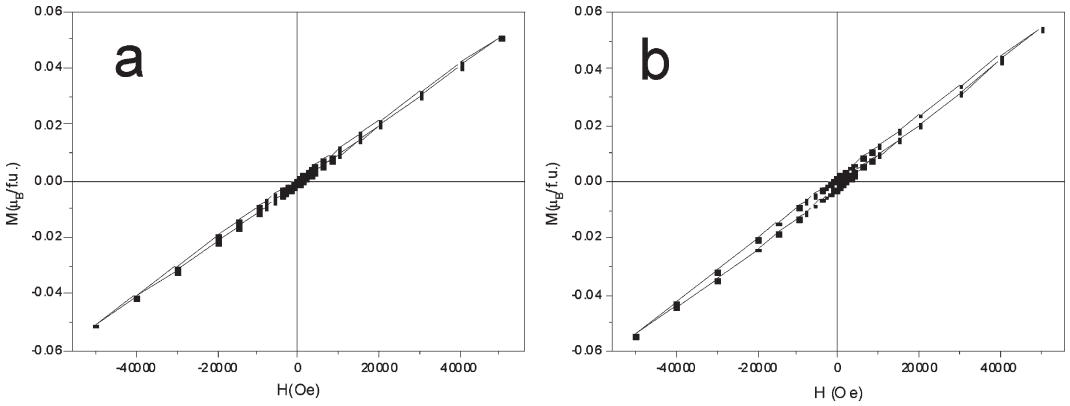


**Figure 8.** Magnetization versus magnetic field at 2 K for (a) $BaMn_{0.85}Fe_{0.15}O_{2.87}$ and (b) $BaMn_{0.60}Fe_{0.40}O_{2.72}$.

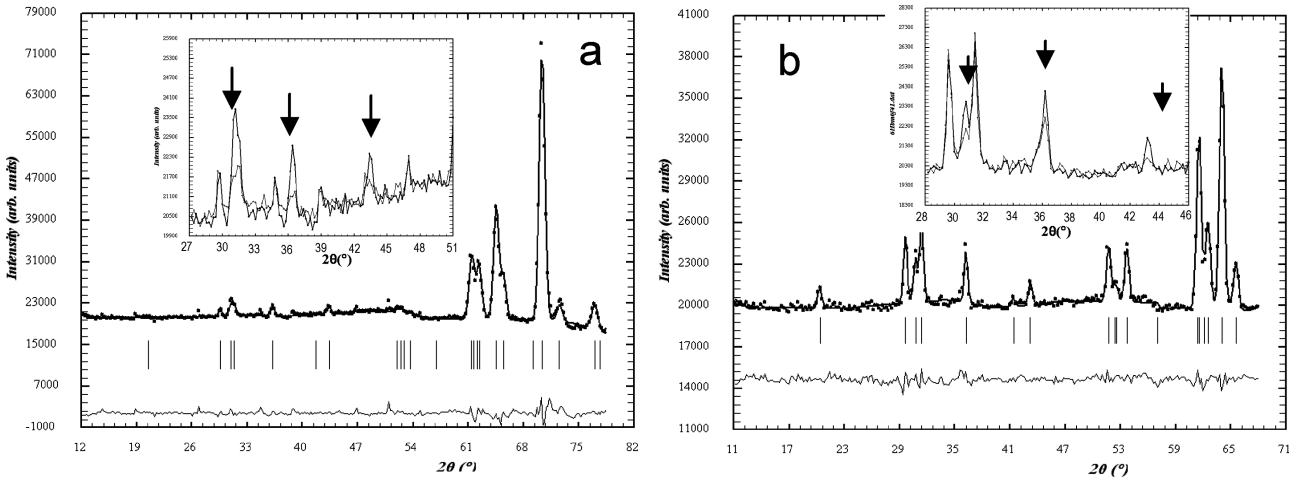


**Figure 9.** Fitting of the neutron diffraction data for (a) $BaMn_{0.85}Fe_{0.15}O_{2.87}$ ($R_B = 5.67$, $R_{mag} = 6.43$, $\chi^2 = 3.16$) and (b) $BaMn_{0.60}Fe_{0.40}O_{2.72}$ ($R_B = 4.57$, $R_{mag} = 7.37$, $\chi^2 = 3.45$) at 2 K.

origin and could be accounted for by the $P\bar{6}m2$ space group with a magnetic unit cell of the same dimensions as the structural one (propagation vector, $k = 0$).

The atomic coordinates were fixed and only the lattice parameters, profile parameters, and magnetic moments were refined. Initially, only Mn was considered to take part in the long-range magnetic ordering. This had been observed previously in 15R-$SrMn_{0.9}Fe_{0.1}O_{3-\delta}$[28] where the Fe cation contribution was negligible. However, for the phases studied here, when only the Mn fraction is considered to contribute to the magnetic moment in each crystallographic site (M1, M2, and M3), the refinement allows an extraordinarily large magnetic moment value for the M3 sites (close to 9 $\mu_B$ in $BaMn_{0.6}Fe_{0.4}O_{2.72}$). To avoid this, we have assumed both transition metal cations take part in the long-range magnetic ordering. Because of the different Mn/Fe fractional occupancies, each transition metal site was assigned an independent magnetic moment. Several models were tested; the best fit was obtained from a magnetic model which assumes antiferromagnetic interactions between nearest neighbors (NN). Figure 9a,b shows the fitting for the $BaMn_{0.85}Fe_{0.15}O_{2.87}$ and $BaMn_{0.60}Fe_{0.40}O_{2.72}$ samples at 2 K, respectively. This model results in a magnetic structure consisting of ferromagnetic sheets with the magnetic moments aligned along the *x*-axis and stacked antiferromagnetically perpendicular to the *c*-axis (Figure 10). The saturated magnetic moment at 2 K on each of the metal transition sites for both 6H samples is given in Table 5 and the thermal variation of the magnetic moments per formula unit obtained from the refinement is shown in Figure 11. According to these data, $T_N = 175$ K is obtained for $BaMn_{0.60}Fe_{0.40}O_{2.72}$ and 275 K for $BaMn_{0.85}Fe_{0.15}O_{2.87}$. These results are consistent with the observed divergence between FC and ZFC data of the magnetic susceptibility (Figure 7).

The value of the refined magnetic moments on each site at 2 K (see Table 5) are lower than the predicted value for $Mn^{4+}$ allowing for a degree of covalency,[29] ca. 2.6 $\mu_B$. This feature is also observed in all the above-mentioned Mn-phases, and it has been ascribed to partial magnetic frustration, originating from competing interactions in some metallic sites occupied by both Fe and Mn ions. Actually, the random distribution of Mn and Fe over the M1 and M3 sites allows the following 90 or 180° superexchange interactions via bridging oxygen, e.g.: $Mn^{IV}(d^3)$−O-$Mn^{IV}(d^3)$, $Fe^{III}(d^5)$−O-$Fe^{III}(d^5)$, $Mn^{IV}(d^3)$−O-$Fe^{III}(d^5)$ along the chain. Considering the first two are

(28) Cussen, E.; Sloan, J.; Vente, J. F.; Battle, P. D.; Gibb, T. C. *Inorg. Chem.* **1998**, *37*, 6071.

(29) Tofield, B. C.; Fender, B. E. F. *J. Phys. Chem. Solids* **1970**, *31*, 2741.

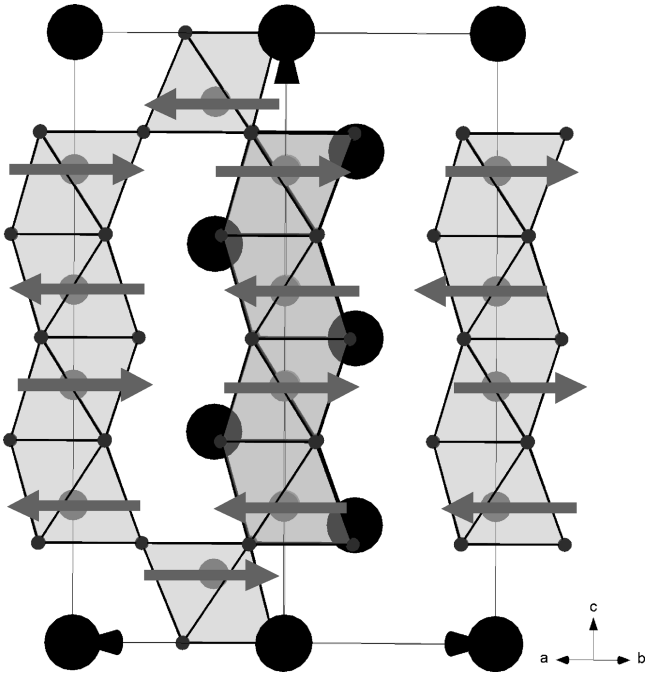


**Figure 10.** Antiferromagnetic structure of 6H′-$BaMn_{1-x}Fe_xO_{3-y}$ ($x$ = 0.15 and 0.40).

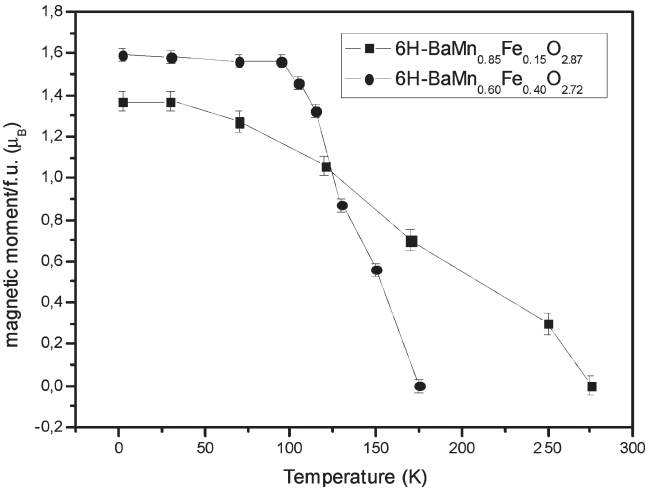


**Figure 11.** Thermal variation of the magnetic moments per formula unit obtained from the refinement corresponding to $BaMn_{0.85}Fe_{0.15}O_{2.87}$ and $BaMn_{0.60}Fe_{0.40}O_{2.72}$.

antiferromagnetic but the latter is ferromagnetic (see Goodenough[30]), competing interactions could be present leading to magnetic frustration which may be responsible for the hysteresis loop observed at 2 K (Figure 8).

6H′-$BaMn_{0.85}Fe_{0.15}O_{2.87}$ has a similar Néel temperature to that of 6H′-$BaMnO_{2.92}$;[4] however, when the amount of Fe increases, for example, $BaMn_{0.60}Fe_{0.40}O_{2.72}$, a lower $T_N$ value is obtained. This decrease in antiferromagnetic ordering temperature maybe due to the magnetic disorder discussed above giving rise to competing magnetic interactions caused by Fe cations.

These results depict a complex behavior for both samples. At room temperature, the magnetic moments of the transition metal cations inside the blocks of face-sharing octahedra are antiferromagnetically coupled leading to short-range order. The magnetic transition at the Néel temperature represents the formation of the long-range magnetically ordered structure described above. On cooling, magnetic frustration can be overcome and the nonordered moments give rise to the increase in susceptibility below 50 K (Figure 7) and the hysteresis loop at 2 K (Figure 8).

(30) *Magnetism and the Chemical Bond*; Goodenough, J. B., Ed.; John Wiley and Sons: New York−London, 1963.

**Table 5. Magnetic Moment for each M-site at 2 K for $BaMn_{0.85}Fe_{0.15}O_{2.87}$ and $BaMn_{0.6}Fe_{0.4}O_{2.72}$**

| | M1 ($\mu_B$) | M2 ($\mu_B$) | M3 ($\mu_B$) | $M_{Total}$ ($\mu_B$/f.u.) |
|---|---|---|---|---|
| $BaMn_{0.85}Fe_{0.15}O_{2.87}$ | 1.20(3) | 0.90(3) | 2.00(3) | 1.37(3) |
| $BaMn_{0.6}Fe_{0.4}O_{2.72}$ | 1.40(3) | 1.07(3) | 2.22(3) | 1.56(3) |

It is worth noting this magnetic model is rather common in Mn-containing hexagonal polytypes with mixed hexagonal and cubic layers. Isostructural 6H′-$BaMnO_{2.92}$[4] adopts the same magnetic structure indicating the partial Mn-substitution for Fe does not modify significantly the magnetic cation arrangement. Moreover, a similar magnetic model is obtained in other Mn-based hexagonal polytypes regardless of the particular stacking sequence(s). For instance, 4H-$BaMnO_3$[24] and 15R-$SrMn_{0.9}Fe_{0.1}O_{3-\delta}$[28] have a similar arrangement scheme with antiferromagnetic interactions in the face-sharing octahedral blocks giving rise to ferromagnetic sheets perpendicular to the $c$-axis. However, this 3D order is not found in 2H-$BaMnO_3$[21] (only hexagonal layers), despite the antiferromagnetic coupling between $Mn^{4+}$ ions in the rows of face-sharing octahedra. This result should be indicative that the general features of the magnetic model proposed for these 6H′-$BaMn_{1-x}Fe_xO_{3-\delta}$ phases may be general behavior in all of the hexagonal polytypes with NN antiferromagnetic interactions between transition metal cations.

## Electrical Properties

Impedance spectroscopy (IS), fixed frequency capacitance, and dielectric loss measurements were performed on ceramics of $BaMn_{0.85}Fe_{0.15}O_{2.87}$ (~93% of the theoretical X-ray density) and $BaMn_{0.6}Fe_{0.4}O_{2.72}$ (~75% of the theoretical density). Room temperature measurements show the ceramics to be semiconducting ($\sigma_{x=0.15} \approx 4.2$ $\mu$S·cm and $\sigma_{x=0.40} \approx 24$ $\mu$S·cm); therefore, subambient temperature measurements were required to obtain meaningful data.

The temperature dependence of the permittivity ($\varepsilon$) was measured at 1, 10, and 100 kHz and at 1 MHz (Figure 12). At low temperature, $\varepsilon$ is frequency independent in both samples giving rise to a plateau with a value of ~15 for $BaMn_{0.6}Fe_{0.4}O_{2.72}$ and ~19 for $BaMn_{0.85}Fe_{0.15}O_{2.87}$. Above 80 and 100 K, $\varepsilon$ and $\tan\delta$ increase significantly in both compounds. The increase in $\tan\delta$ is clearly higher for $x = 0.40$, indicating that leakage conductivity is much higher in this compound compared to $x = 0.15$. $\varepsilon$ at room temperature for both compounds is ~120 at 1 kHz but is frequency dependent. Such behavior is indicative of an extrinsic effect and will be discussed later. The low

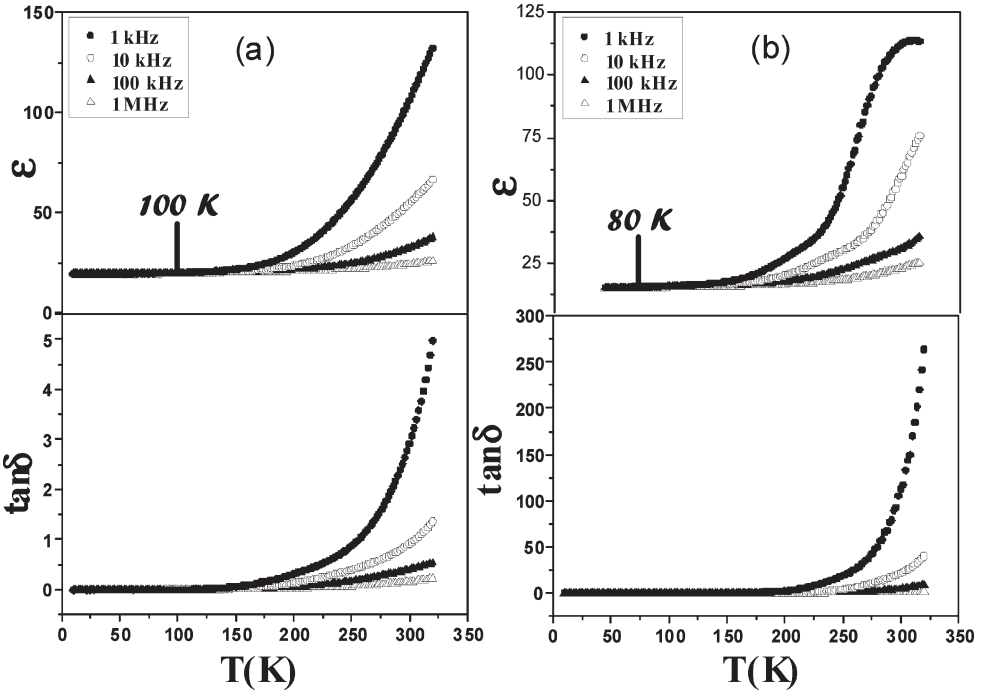


**Figure 12.** Temperature dependence of the permittivity ($\varepsilon$) and dielectric losses of (a) $BaMn_{0.85}Fe_{0.15}O_{2.87}$ and (b) $BaMn_{0.60}Fe_{0.40}O_{2.72}$.

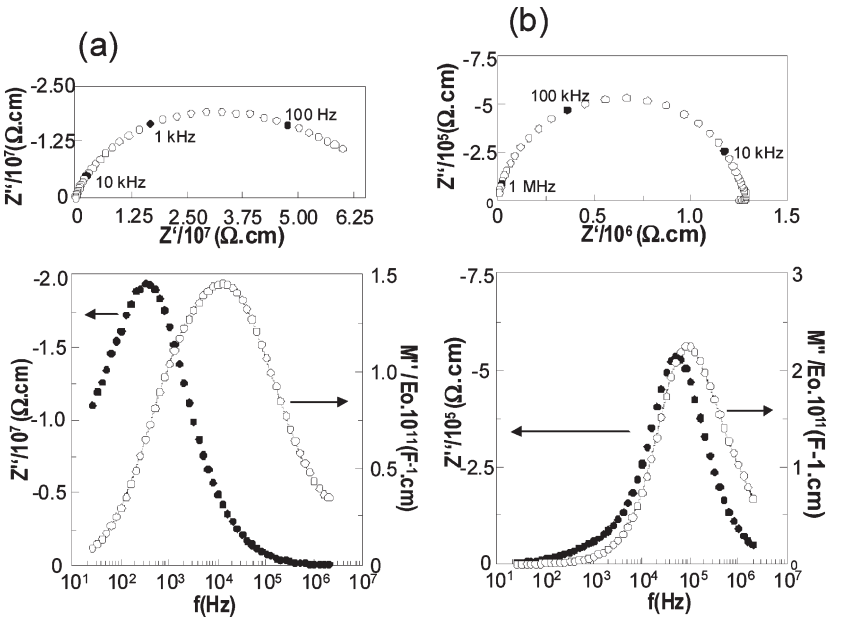


**Figure 13.** Z* impedance plot and M″/Z″ spectroscopic plot at 250 K of (a) $BaMn_{0.85}Fe_{0.15}O_{2.87}$ and (b) $BaMn_{0.60}Fe_{0.40}O_{2.72}$.

temperature permittivity value of ~15 to 20 for both compounds is related to the bulk response of the ceramics and represents the intrinsic or relative permittivity ($\varepsilon_r$) of these compounds. To clarify the origin(s) of the apparent rise in $\varepsilon$ at room temperature and its frequency dependency, IS was performed on the ceramics.

Combined Z″ and M″ spectroscopic plots for the ceramics at 250 K are shown in Figure 13. These plots are representative of the IS data collected at subambient temperatures for the samples. $BaMn_{0.85}Fe_{0.15}O_{2.87}$ ceramic display clear evidence of electrical heterogeneity with a single Debye-like peak in the Z″ spectrum but a broadened M″ peak with a half height peak width in excess of 3 decades on a log f scale (Figure 13a). The Z″ and M″ peak maxima are not coincident and are separated by nearly 2 orders of magnitude. The IS data were therefore modeled on a combination of two parallel resistor−capacitor ($R-C$) elements connected in series with one element being represented by the Z″ peak and the other by the M″ peak. $R$ and $C$ values for each element were estimated using the relationship $\omega RC = 1$ (where $\omega = 2\pi f$ and $f$ is the frequency in Hz) at the peak maxima. The magnitude of $C$ associated with the $M''$ peak was ~2 to 3 $pFcm^{-1}$ ($\varepsilon'$ ~20 to 30) which is consistent with a bulk (or grain) response and is in good agreement with the values of ~15 to 20 obtained from the low temperature,

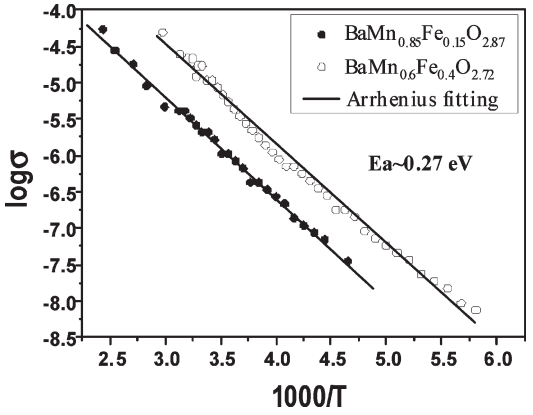


**Figure 14.** Arrhenius plot of the bulk conductivity ($\sigma_b = 1/R$) for $BaMn_{0.85}Fe_{0.15}O_{2.87}$ and $BaMn_{0.60}Fe_{0.40}O_{2.72}$.

fixed frequency capacitance measurements (Figure 12). The values obtained from the M″ spectra are an overestimation owing to the nonideal Debye peak associated with the grain response. Nevertheless the agreement in the magnitude of the permittivity is sufficient to confirm the M″ spectra are associated with the bulk response.

An Arrhenius plot of the bulk conductivity ($\sigma_b = 1/R$) obtained from the M″ spectra show a linear response over the measured temperature range with the activation energy, $E_a$, for the bulk conduction to be ~0.27 eV (Figure 14). The magnitude of the capacitance associated with the Z″ peak was ~20 pFcm$^{-1}$ ($\varepsilon' \approx 200$). The conductivity data (not shown) associated with the Z″ spectra also obeyed the Arrhenius law with $E_a$ ~0.3 eV; however, it was ~$^1/_2$ an order of magnitude lower than the bulk conductivity obtained from the M″ spectra. This suggests the conduction mechanism in this element is the same as the bulk conduction mechanism; albeit with a lower carrier concentration. Given the high density of this ceramic (~93%) it is unlikely that the response associated with the Z″ spectra is a constriction resistance associated with incomplete sintering[31] and therefore, it is attributed to a resistive, shell-type, outer region on individual grains. Thus, the electrical heterogeneity of this ceramic is associated with the existence of oxygen concentration gradients within the grains of the ceramic. This proposed explanation is consistent with the chemical processing employed to produce dense ceramics from the $BaMn_{0.85}Fe_{0.15}O_{2.87}$ powder. The powder was prepared by a solid state reaction route that required high processing temperatures (1648 K) followed by rapid quenching to room temperature. In an attempt to maintain this composition, and in particular the oxygen-content, the sintering process employed for the ceramics was the same as that used to produce the powder. Diffusion of oxygen into the grains of the dense ceramics on cooling will have been restricted via diffusion along the grain boundaries. The outer regions of the grains (shells) are likely, therefore, to have a higher oxygen-content compared to the inner regions of the grains (cores). Such core−shell electrical microstructures are commonly obtained in transition metal oxide containing ceramics that have been rapidly cooled from high sintering temperatures.[32]

In contrast, the IS data for $BaMn_{0.6}Fe_{0.4}O_{2.72}$ ceramics show near ideal and coincident, single Debye-like Z″ and M″ peaks, Figure 13b. The data could be modeled on a single, parallel *RC* element. The associated capacitance of the M″ peak was 2.2−2.4 pFcm$^{-1}$ ($\varepsilon \approx 23$), therefore confirming this to be the bulk response. An Arrhenius plot of the bulk conductivity shows a linear response with $E_a \approx 0.27$ eV. The conduction mechanism is therefore the same as that observed for $BaMn_{0.85}Fe_{0.15}O_{2.87}$. The higher conductivity of the $x = 0.40$ sample is attributed to the higher ratio of mixed valent Mn in this sample, that is, a $Mn^{3+}$:$Mn^{4+}$ ratio of 1:3 compared with 1:7 for $x = 0.15$. The conduction mechanism is likely to be a localized electron-hopping model associated with the mixed valence of the Mn-ions in these compounds. The homogeneous electrical microstructure for $BaMn_{0.6}Fe_{0.4}O_{2.72}$ and therefore homogeneous oxygen distribution within the ceramics is attributed to the lower density of ceramics (~73%). The presence of open porosity within ceramics ensures better solid−gas equilibration between the ceramic and the atmosphere on cooling compared to the limited diffusion of oxygen in the grain boundaries for dense ceramics. The difference in ceramic microstructure of the samples, that is, pellet density, therefore plays a significant role in controlling the electrical microstructure, that is, the occurrence and distribution of oxygen concentration gradients within individual grains of the ceramics.

The bulk permittivity values for these samples are < 20. This value is similar to that obtained for the 10H sample (< 20),[10] but is lower than that of 12R $Ba(Ti,Mn)O_3$[12,14] and 6H-$BaTiO_3$.[23] This is expected, given the higher polarizability of Ti ions compared to Fe and Mn. The permittivity values can therefore be understood on the basis of the Clausius−Mossotti (C−M) equation where the permittivity is related directly to the sum of the ion polarizability of the ions in the unit cell and inversely related to the unit cell molar volume. Calculations show the expected permittivity, $\varepsilon_{CM}$, based on the C−M equation to be 15.5 and 16.0 for $x = 0.15$ and 0.40, respectively. These values are in excellent agreement with the experimental values obtained from the low temperature, fixed frequency capacitance, and IS measurements. Although not shown, it is noteworthy that the bulk permittivity of these samples showed little temperature dependence and did not show any anomaly at their respective Néel temperatures. No significant magnetoelectric coupling is therefore likely to be present in these materials.

In conclusion, the 6H′ structural characterization of two new Mn-rich 6H′ phases within the $BaMn_{1-x}Fe_xO_{3-\delta}$ system, $BaMn_{0.85}Fe_{0.15}O_{2.87}$ and $BaMn_{0.6}Fe_{0.4}O_{2.72}$, has been established. The structure is formed by tetramers and dimers of face-sharing octahedra that

(31) Bruce, P. G.; West, A..R. *J. Electrochem. Soc.* **1983**, *130*, 662.

(32) Álvarez Roca, R.; Botero, E. R.; Guerrero, F.; Guerra, J. D. S.; García, D.; Eiros, J. A. *J. Phys. D: Appl. Phys.* **2008**, *41*, 045410.

are linked by corners. In both phases, the central position of the tetramers is fully occupied by Mn. The remaining Mn and Fe cations are randomly distributed. The anionic deficiency is randomly distributed in the hexagonal layers and increasing with the Fe-content. This is in agreement with Mössbauer spectroscopy data that are consistent with $Fe^{3+}$ in octahedral and tetrahedral coordination. Neutron diffraction data suggest a complex magnetic structure formed by ferromagnetic sheets with the magnetic moments aligned along the *x*-axis and stacked antiferromagnetically perpendicular to the *c*-axis. At room temperature, the magnetic moments of the cations inside the blocks of face-sharing octahedra are antiferromagnetically coupled leading to short-range order. Both compounds behave as leaky insulators at room temperature with bulk permittivity values $< 20$.

**Acknowledgment.** Financial support through research project MAT2007-61954 (Madrid), S0505/PPQ/0316 (CAM), FAME-NoE FP6-500159 (Madrid, Sheffield) and EPSRC (Sheffield) is acknowledged. We thank Dra. M.T. Fernández-Díaz for assistance in collecting the neutron powder diffraction data.